Autotuned Nonlinear Extended State Observer-Based Fixed-Time Control for Motor-Drive Servo Systems

Ruiqi Xu, *Graduate Student Member, IEEE*, Jianxing Liu, *Senior Member, IEEE*, Xinpo Lin, *Member, IEEE*, Zhuang Liu, *Member, IEEE*, Fei Yan, *Member, IEEE*, and Yabin Gao, *Member, IEEE*

***Abstract*—To enhance the position tracking performance of permanent magnet synchronous motors (PMSMs) under unknown disturbances, this article proposes a fast fixed-time control strategy based on an improved nonlinear extended state observer (NESO). First, load disturbances and nonlinear friction are considered as lumped disturbance, for which an NESO is designed to estimate the lumped disturbance. The control parameters of the NESO are tuned online using a neural network optimization algorithm, eliminating the need for offline training. Then, a robust fixed-time sliding mode control method is proposed, based on an improved nonsingular fast terminal sliding mode manifold, which offers better convergence performance. The Lyapunov method is used to prove the fixed-time stability of the position tracking error system. Finally, the effectiveness of the proposed method is validated on an experimental platform with PMSMs, and it is compared with other advanced fixed-time position control methods. The comparison results confirm that the proposed method exhibits superior control performance.**

***Index Terms*—Fixed-time control, nonlinear extended state observer (ESO), parameter optimization, permanent magnet synchronous motor (PMSM).**

Nomenclature

i_d, i_q	dq-axis stator currents.
u_d, u_q	dq-axis stator voltages.
L_d, L_q	dq-axis stator inductance.
p_n	Number of pole pairs.
ψ_f	Flux linkage.
T_e	Electromagnetic torque.
ω	Mechanical angular velocity.
ω_e	Electrical angular velocity.
T_L	Load torque.
J	Moment of inertia.
B	Viscous friction coefficient.
R_s	Stator resistance.

Received 22 October 2024; revised 19 March 2025; accepted 18 April 2025. Date of publication 1 May 2025; date of current version 5 August 2025. This work was supported in part by the National Natural Science Foundation of China under Grant 62373127, Grant 62403168, Grant 62373311, Grant 62473118, and Grant 62320106001, and in part by the China Postdoctoral Science Foundation under Grant 2024M764189. Recommended for publication by Associate Editor H. H.-C. Iu. *(Corresponding author: Jianxing Liu.)*

Ruiqi Xu, Jianxing Liu, Zhuang Liu, and Yabin Gao are with the Department of Control Science and Engineering, Harbin Institute of Technology, Harbin 150001, China (e-mail: jx.liu@hit.edu.cn).

Xinpo Lin is with the Department of Control Science and Engineering, Harbin Institute of Technology, Weihai 264209, China.

Fei Yan is with the School of Information Science and Technology, Southwest Jiaotong University, Chengdu 611756, China.

Color versions of one or more figures in this article are available at https://doi.org/10.1109/TPEL.2025.3566215.

Digital Object Identifier 10.1109/TPEL.2025.3566215

I. Introduction

PERMANENT magnet synchronous motors (PMSMs) are widely employed in servo control systems because of their efficiency, precision, and reliability [1]. In such systems, the accuracy and response speed of the controller are pivotal factors that directly influence the overall performance and efficiency. However, the PMSMs system are nonlinear and easily affected by disturbances and uncertainties, including variations in unknown dynamics, friction, and external load disturbances.

Recently, numerous nonlinear control methods have been developed to improve position control performance for PMSMs. In [2], an active disturbance rejection control (ADRC) was applied to the position servo system, providing a simple structure and robust performance. However, ADRC was limited by the numerous parameters and their intricate interdependencies, which make parameter optimization a challenging task. To address this issue, researchers have explored various parameter optimization methods. A parameter optimization method based on optimal control theory was proposed in [3], which addressed the tradeoff between high gain and measurement noise in the extended state observer (ESO). However, this method encountered additional challenges in complex nonlinear systems, including unclear relationships between parameters and sensitivity to initial values. The emergence of heuristic algorithms provided innovative solutions to parameter optimization challenges. In [4], particle swarm optimization (PSO) was employed to derive optimized sliding mode control gains by addressing a tradeoff optimization problem between the ultimate bound and the communication burden. In [5], an improved quantum genetic algorithm (GA) was proposed to optimize PID control. In [6], an adaptive data-driven iterative feedforward tuning method based on a fast recursive algorithm was proposed. This method simultaneously tunes both the structure and parameters of the feedforward controller. In [7], a weighting factors optimization method was proposed, which utilized an aggregated residual network that combined the advantages of residual connections and aggregated transformations. In [8], an online parameter identification framework based on deep reinforcement learning (DRL) was proposed. This framework utilized a DRL agent capable of learning the ADRC policy through the construction of a training scenario database in an offline manner. While the algorithms demonstrated

effectiveness, they were burdened by significant computational demands, particularly in the cases of PSO [4] and GA [5]. In addition, knowledge-based methods required a large dataset for offline training [6], [7], [8]. These existing issues served as the impetus for this research.

In servo control systems, such as industrial robotic arms moving along a production line, stringent time response requirements were essential to ensure safety and enhance productivity. Conventional nonlinear controls, such as terminal sliding mode and higher order sliding mode, were limited to achieving finite-time convergence, with the settling time being contingent upon the initial conditions [9]. The fixed-time stabilization control was first proposed in [10], where the settling-time was bounded by control gains and independent of initial conditions. In [11], a fixed-time controller was designed using a double limit homogeneous method to improve the dynamic performance of PMSM. However, this method had relatively high computational complexity. In [12], the convergence rate of the system was significantly enhanced by employing a fixed-time command filter control approach. The system's convergence under predefined performance criteria was achieved through the design of an adaptive fuzzy fixed-time control in [13]. In [14], an adaptive quasi-fixed-time terminal sliding mode control was proposed, which accelerates the system's convergence rate but faces singularity issues. In [15], the singularity issue is circumvented by leveraging the intrinsic properties of the saturation function. Meanwhile, in [16], [17], and [18], fixed-time integral sliding manifolds were constructed to ensure the convergence of system errors within a fixed-time frame, thereby effectively addressing the singularity challenge. In [19] and [20], dual-layer fixed-time sliding mode manifolds were designed to guarantee the convergence of system errors within a fixed time, effectively reducing chattering. However, this approach results in an increase in the upper bound of the convergence time. The design of a variable-gain nonsingular terminal sliding mode manifold, as proposed in [21], [22], and [23], has been demonstrated to effectively enhance the convergence rate. In [24], [25], [26], and [27], the singularity issue was addressed, and a variable-exponent fixed-time stable system was designed, further increasing the convergence speed. Although the aforementioned efforts have made significant strides in enhancing the convergence performance of fixed-time control, it remains crucial to further explore methods with faster convergence speeds to improve the system's robustness, dynamic response, and static performance.

Motivated by the above observations, this article designs an ESO-based parameter self-tuning mechanism and a fast fixed-time sliding mode control (FFTSMC) method. The main contributions of this article are listed as follows:

1) The designed nonlinear extended state observer (NESO) employs neural networks for real-time parameter autotuning. The designed neural network algorithm can learn and update parameters from real-time and historical data, enhancing the system's adaptability to the environment. In comparison to existing literature [6], [7], the proposed algorithm eliminates the need for offline data acquisition and training.
2) The designed FFTSMC utilizes a nonsingular fast terminal sliding mode manifold so that the system converges within a fixed time and is independent of the initial state. In comparison to existing literature [26], [27], the proposed novel fixed-time stabilization system has a faster convergence rate.
3) The experimental results demonstrate that the NESO-based FFTSMC improves the steady-state performance and anti-interference capability of the PMSM servo system compared to fixed-time position control methods proposed in [28].

II. System Description and Preliminaries

A. Mathematical Model

The mechanical equation of the IPMSM is expressed as [29]

$$\begin{aligned}\frac{d\omega}{dt} &= \frac{T_e}{J} - \frac{B}{J}\omega - \frac{T_L}{J}\\ T_e &= \frac{3}{2}p_n i_q[i_d(L_d - L_q) + \psi_f].\end{aligned} \tag{1}$$

The state variables of the system are defined as follows:

$$\begin{cases} x_1 = \theta - \theta^* \\ x_2 = \dot{x}_1 = \omega - \dot{\theta}^* \end{cases} \tag{2}$$

where θ and θ^* represent actual mechanical position and reference position signal, respectively.

Combining (1) and (2), the state variables are expressed as

$$\begin{cases} \dot{x}_1 = \omega - \dot{\theta}^* \\ \dot{x}_2 = \frac{3p_n}{2J}[i_d(L_d - L_q) + \psi_f]i_q - \frac{B}{J}\omega - \frac{T_L}{J} - \ddot{\theta}^*. \end{cases} \tag{3}$$

The reference i_d^* is set to 0 to simplify the control [30]. If the controller of i_d loop works well, one obtains $i_d^* = i_d = 0$. Then, the state variables are then rewritten as follows:

$$\begin{cases} \dot{x}_1 = \omega - \dot{\theta}^* \\ \dot{x}_2 = \chi i_q + d - \ddot{\theta}^* \end{cases} \tag{4}$$

where $\chi = \frac{3}{2J}p_n\psi_f$, and d represents the lumped disturbance.

Assumption 1 (See [30]): There is an upper bound on both the lumped disturbance $d(t)$ and its time derivative, which are denoted by $|d| \le D_1$ and $|\dot{d}| \le D_2$. D_1 and D_2 are two positive constants.

Remark 1: In general, control inputs, external perturbations, nonlinear friction, and the unknown dynamics of real systems are all restricted within a certain operational range, thereby making the lumped perturbation essentially bounded.

B. Extended State Observer

Considering the lumped disturbance of system (4), ESO is designed to estimate the disturbance. The NESO is designed as

follows:

$$\begin{cases} e_1 = \hat{\theta} - \theta \\ \dot{\hat{\theta}} = \hat{\omega} - \beta_1 \cdot fal(e_1) \\ \dot{\hat{\omega}} = \chi i_q + \hat{d} - \beta_2 \cdot fal(e_1) \\ \dot{\hat{d}} = -\beta_3 \cdot fal(e_1) \end{cases} \tag{5}$$

where the symbol $\hat{\cdot}$ is the estimated value of the corresponding variable, e_1 is the error the estimated and actual rotor position, and $\beta_i (i = 1, 2, 3)$ are positive parameters to be determined. The function $fal(\cdot)$ is nonlinear exponential function expressed as

$$fal(e) = \begin{cases} \frac{e}{\delta^{1-\alpha}}, & |e| \le \delta \\ |e|^{\alpha} \cdot \text{sign}(e), & |e| > \delta. \end{cases} \tag{6}$$

The tuning of parameter $\beta_i (i = 1, 2, 3)$ directly impacts the ESO's observation of the system state and the overall internal and external perturbations. Stability analysis has been proven in detail in [31], and state estimation errors $e_i (i = 1, 2, 3)$ meet the following conditions in finite time T_r:

$$|e_i| \le M,\ i = (1, 2, 3),\ M > 0. \tag{7}$$

C. Preliminary Lemmas

Lemma 1 (See [26]): If the following system satisfies:

$$\dot{y} = -\alpha \text{sig}^{k_1}(y) - \beta \text{sig}^{k_2}(y) \tag{8}$$

where $k_1 = m_1^{\text{sign}(|y|-1)}$, $k_2 = m_2^{\text{sign}(1-|y|)}$, $m_1 = m/n$, $m_2 = p/q$, $\alpha > 0$, $\beta > 0$, and $\text{sig}^k(y) = |y|^k \text{sign}(y)$. m, n, p, and q are positive odd integers that satisfy $m > n$ and $p < q$. Then, the system (8) is fixed-time stable, and the maximum of setting time can be calculated by

$$\begin{aligned} T_{\max} = &\min\left\{ \frac{1}{\beta(m_1 - 1)} \ln\left(1 + \frac{\beta}{\alpha}\right), \frac{m_2}{\alpha(1 - m_2)} \ln\left(1 + \frac{\alpha}{\beta}\right) \right\} \\ &+ \min\left\{ \frac{1}{\beta(1 - m_2)} \ln\left(1 + \frac{\alpha}{\beta}\right), \frac{m_1}{\alpha(m_1 - 1)} \ln\left(1 + \frac{\beta}{\alpha}\right) \right\}. \end{aligned} \tag{9}$$

Lemma 2 (See [27]): If the following system satisfies:

$$\dot{y} = -\frac{1}{\mu(y)} \left(\alpha \text{sig}^{k}(y) + \beta \text{sig}^{\frac{p}{q}}(y) \right) \tag{10}$$

where $\mu(y) = a_1 + (1 - a_1)\exp(-a_2 |y|^{a_3})$, $k = 1/2 + \frac{m}{2n} + (\frac{m}{2n} - 1/2)\text{sign}(|y| - 1)$, $\alpha > 0$, $\beta > 0$, $0 < a_1 < 1$, $a_2 > 0$, $a_3 > 0$ is an even integer. m, n, p, and q are positive odd integers that satisfy $m > n$ and $p < q$. Then, the system (10) is fixed-time stable and the maximum of setting time can be calculated by

$$T_{\max} = \frac{n}{\alpha(m - n)} + \frac{q}{\alpha(q - p)} \ln\left(1 + \frac{\alpha}{\beta}\right). \tag{11}$$

Lemma 3: If the following system satisfies:

$$\dot{y} = -\frac{1}{\mu(y)} \left(\alpha \text{sig}^{k_1}(y) + \beta \text{sig}^{k_2}(y) \right) \tag{12}$$

where $\mu(y) = a_1 + (1 - a_1)\exp(-a_2 |y|^{a_3})$, $k_1 = 1 + \frac{m}{2n}(1 + \text{sign}(|y| - 1))$, $k_2 = \frac{1}{2}(1 + \frac{p}{q}) + \frac{1}{2}(1 - \frac{p}{q})\text{sign}(|y| - 1)$, $\alpha > 0$, $\beta > 0$, $0 < a_1 < 1$, $a_2 > 0$, and $a_3 > 0$ is an even integer. m, n, p, and q are positive odd integers that satisfy $m > n$ and $q > p$. Then, the system (12) is fixed-time stable, and the maximum settling time can be calculated by

$$T_{\max} = \frac{n}{\beta m} \ln\left(1 + \frac{\beta}{\alpha}\right) + \frac{q}{\alpha(q - p)} \ln\left(1 + \frac{\alpha}{\beta}\right). \tag{13}$$

Proof: (12) can be rewritten as

$$\begin{cases} \dot{y} = -\frac{1}{\mu(y)} \left(\alpha \text{sig}^{1 + m/n}(y) + \beta y \right), & |y| > 1 \\ \dot{y} = -\frac{1}{\mu(y)} \left(\alpha y + \beta \text{sig}^{p/q}(y) \right), & |y| \le 1. \end{cases} \tag{14}$$

For case 1: $|y| > 1$, introducing a variable as $z = 1 + \ln|y|$, and for case 2: $|y| \le 1$, introducing a variable as $z = |y|^{1 - p/q}$. Then, (14) can be written as

$$\begin{cases} \dot{z} = -\frac{1}{\mu(y)} \left(\alpha e^{(z-1)(m/n)} + \beta \right), & |z| > 1 \\ \dot{z} = -\frac{1}{\mu(y)} \left(\alpha z (1 - p/q) + \beta (1 - p/q) \right), & 0 < |z| \le 1. \end{cases} \tag{15}$$

By solving it, the convergence time can be calculated as

$$\begin{aligned} T_{\max} &= \lim_{y(0) \to \infty} T(y(0)) \\ &= \lim_{z_0 \to \infty} \left(\int_1^{z_0} \frac{\mu(y)}{\alpha e^{(z-1)(m/n)} + \beta} dz \right. \\ &\quad \left. + \int_0^{z_1} \frac{\mu(y)}{(1 - p/q)(\alpha z + \beta)} dz \right) \\ &= \lim_{z_0 \to \infty} \int_1^{z_0} \frac{\mu(y)}{\alpha e^{(z-1)(m/n)} + \beta} dz \\ &\quad + \frac{\mu(y) q}{\alpha(q - p)} ln \left(1 + \frac{\alpha}{\beta}\right). \end{aligned} \tag{16}$$

Let $T_1 = \lim_{z_0 \to \infty} \int_1^{z_0} \frac{\mu(y)}{\alpha e^{(z-1)(m/n)} + \beta} dz$ and $\rho = e^{(z-1)(m/n)}$, and then

$$\begin{aligned} T_1 &= \frac{n \mu(y)}{m} \lim_{\rho_0 \to \infty} \int_1^{\rho_0} \frac{1}{\rho(\alpha \rho + \beta)} d\rho \\ &= \frac{n \mu(y)}{m} \lim_{\rho_0 \to \infty} \int_1^{\rho_0} \frac{1}{\rho \beta} - \frac{\alpha}{\beta(\rho \alpha + \beta)} d\rho \\ &= \frac{n \mu(y)}{\beta_o m} \ln\left(1 + \frac{\beta_o}{\alpha_o}\right). \end{aligned} \tag{17}$$

Since $\mu(y) \le 1$, the settling time can be rewritten as

$$T_{\max} = \frac{n}{\beta m} \ln\left(1 + \frac{\beta}{\alpha}\right) + \frac{q}{\alpha(q - p)} \ln\left(1 + \frac{\alpha}{\beta}\right). \tag{18}$$

The proof is completed.

To verify the fast convergence of the proposed fixed-time stable system, a comparison is made with a typical fixed-time stable system [26], [27] using the same controller parameters. $\alpha = \beta = 2$, $m = 9$, $n = 5$, $p = 7$, $q = 9$, $a_1 = 0.8$, $a_2 = 10$, and $a_3 = 2$. From Fig. 1, it can be observed that the proposed method achieves faster fixed-time convergence compared to the existing fixed-time stable system.

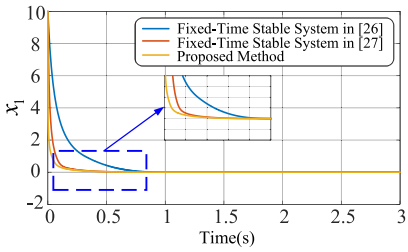

Fig. 1. Convergence rate under different fixed-time methods.

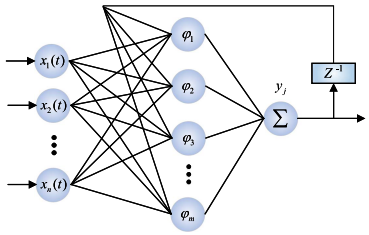

Fig. 2. Block diagram of the neural network-based NESO parameter tuning design.

III. Proposed Control Method

A. Parameter Tuning Based on Neural Network

By capitalizing on the robust nonlinear mapping and global approximation capabilities inherent in neural networks, the NESO parameters are dynamically tuned online via neural networks to enhance the adaptability of the controller. The neural network comprises a conventional three-layer feed-forward architecture consisting of an input layer, a hidden layer, and an output layer. To visually clarify the network's structure, Fig. 2 depicts it for illustrative purposes.

In Fig. 2, $x = [x_1, x_2, \ldots, x_n]$ is the input neuron, $\varphi = [\varphi_1, \varphi_2, \ldots, \varphi_m]$ is the hidden layer activation function, $w = [w_1, w_2, \ldots, w_m]$ is the hidden layer weight vector, and $y = [y_1, y_2, \ldots, y_p]$ is the output neuron.

The hidden layer activation function adopts Gaussian function, whose expression is as follows:

$$\varphi(x(k)) = \exp\left(-\frac{\|x(k) - c_i(k-1)\|^2}{2b_i^2(k-1)}\right) \quad i = 1, 2, \ldots, m \tag{19}$$

where $c_i = [c_1, c_2, \ldots, c_N]$ is the Gauss center point of the ith hidden layer neuron, b_i is the base width length of the ith hidden layer node, which is used to adjust the sensitivity of the neuron, $\|\cdot\|$ is the Euclidean norm, which represents the distance between the input neuron and the central point vector.

The output layer expression is

$$y_j(k) = \sum_{i=1}^{m} w_{ij}(k-1)\varphi_j\left(x(k)\right) \quad j = 1, 2, \ldots, p \tag{20}$$

where $w_{ij}(k-1)$ is the output weight of the ith hidden layer neuron at the $k-1$th instant.

The training error is defined as

$$e_j(k) = y_{\text{out}}(k) - y_j(k) \tag{21}$$

where y_{out} is the actual output of the control system. Define the approximation performance index function based on (21) as follows:

$$E(k) = \frac{1}{2}\sum_{j=1}^{p} e_j^2(k). \tag{22}$$

The combination of (21) and (22) can be

$$\frac{\partial E(k)}{\partial y_j(k)} = \frac{\partial E(k)}{\partial e_j(k)} \cdot \frac{\partial e_j(k)}{\partial y_j(k)} = -e_j(k). \tag{23}$$

Combining (20) and (23), based on the gradient descent method, the update equation for $w_{ij}(k)$ is obtained as

$$\frac{\partial E(k)}{\partial w_{ij}(k-1)} = \frac{\partial E(k)}{\partial y_j(k)} \cdot \frac{\partial y_j(k)}{\partial w_{ij}(k-1)} = -e_j(k)\varphi_i\left(x(k)\right) \tag{24}$$

$$\Delta w_{ij}(k) = -\eta\frac{\partial E(k)}{\partial w_{ij}(k-1)} = \eta e_j(k)\varphi_i\left(x(k)\right) \tag{25}$$

$$\begin{aligned} w_{ij}(k) = {} & w_{ij}(k-1) + \Delta w_{ij}(k) \\ & + \alpha\left(w_{ij}(k-1) - w_{ij}(k-2)\right) \end{aligned} \tag{26}$$

where η is learning rate, α is momentum, and $0 < \eta < 1$ and $0 < \alpha < 1$. The combination of (20) and (23) can be

$$\frac{\partial E(k)}{\partial \varphi_i(x(k))} = \frac{\partial E(k)}{\partial y_j(k)} \cdot \frac{\partial y_j(k)}{\partial \varphi_i(x(k))} = -e_j(k)w_{ij}(k-1). \tag{27}$$

The update equation for the center point c_i of the hidden layer is as follows:

$$\begin{aligned} \frac{\partial E(k)}{\partial c_i(k-1)} &= \frac{\partial E(k)}{\partial \varphi_i(x(k))} \cdot \frac{\partial \varphi_i(x(k))}{\partial c_i(k-1)} \\ &= -e_j(k)w_{ij}\varphi_i(x(k))\frac{x(k) - c_i(k-1)}{b_i^2(k-1)} \end{aligned} \tag{28}$$

$$\begin{aligned} \Delta c_i(k) &= -\eta\frac{\partial E(k)}{\partial c_i(k-1)} \\ &= -\eta e_j(k)w_{ij}(k+1)\varphi_i(x(k))\frac{x(k) - c_i(k-1)}{b_i^2(k-1)} \end{aligned} \tag{29}$$

$$\begin{aligned} c_i(k) = {} & c_{ij}(k-1) + \Delta c_{ij}(k) + \alpha(c_{ij}(k-1) \\ & - c_{ij}(k-2)). \end{aligned} \tag{30}$$

The implicit layer base width parameter b_i is updated as follows:

$$\begin{aligned} \frac{\partial E(k)}{\partial b_i(k-1)} &= \frac{\partial E(k)}{\partial \varphi_i(x(k))} \cdot \frac{\|x(k) - c_i(k-1)\|^2}{b_i^3(k-1)} \\ &= -e_j(k)w_{ij}\varphi_i(x(k))\frac{x(k) - c_i(k-1)}{b_i^3(k-1)} \end{aligned} \tag{31}$$

$$\Delta b_i(k) = -\eta\frac{\partial E(k)}{\partial b_i(k-1)}$$

Algorithm 1: Neural Network Parameter Tuning Algorithm.

1: Initialize the parameters in Neural Network, including $w_i(0)$, $c_i(0)$, $b_i(0)$, η, α and parameters to be optimized $\beta_i(i=1,2,3)$
2: for Calculate the incremental coefficients e_{c1}, e_{c2}, e_{c3} from (34)
3: Construct a dynamic neural network and compute the output layer $y_j(k)$ based on (19) and (20);
4: The network parameters $w_{ij}(k)$, $c_i(k)$, $b_i(k)$ are calculated based on (26), (30), and (33);
5: Obtain Jacobian information from the obtained parameters $w_{ij}(k)$, $c_i(k)$, $b_i(k)$ and (36);
6: Update the parameters $\beta_i(i=1,2,3)$ optimized in NESO according to (35);
7: end for

$$= -\eta e_j(k) w_{ij}(k+1)\varphi_i(x(k)) \times \frac{\|x(k)-c_i(k-1)\|^2}{b_i^3(k-1)} \tag{32}$$

$$b_i(k) = b_i(k-1) + \Delta b_i(k) + \alpha\left(b_i(k-1) - b_i(k-2)\right). \tag{33}$$

The 3-6-1 model has been selected to represent the structure of the validated neural network. The input layer vector is $[i_q^* \quad \theta(k) \quad \theta(k-1)]$. By incorporating (21), the incremental coefficients can be defined as follows:

$$\begin{cases} e(k) = \theta(k) - \theta^*(k) \\ e_{c1} = e(k) - e(k-1) \\ e_{c2} = e(k) \\ e_{c3} = e(k) - 2e(k-1) + e(k-2). \end{cases} \tag{34}$$

Combined with (34), the expression for the parameters tuning in the NESO is

$$\begin{cases} \beta_1 = \beta_1(k-1) + \beta_1(k-1)\cdot e \cdot \frac{\partial y_{\text{out}}(k)}{\partial i_q^*(k)} \cdot e_{c1} \\ \beta_2 = \beta_2(k-1) + \beta_2(k-1)\cdot e \cdot \frac{\partial y_{\text{out}}(k)}{\partial i_q^*(k)} \cdot e_{c2} \\ \beta_3 = \beta_3(k-1) + \beta_3(k-1)\cdot e \cdot \frac{\partial y_{\text{out}}(k)}{\partial i_q^*(k)} \cdot e_{c3} \end{cases} \tag{35}$$

where $\partial y_{\text{out}}(k)/\partial i_q^*(k)$ is the Jacobian information of the controlled object, which indicates the sensitivity of the system's input to the output. Its expression is

$$\frac{\partial y_{\text{out}}(k)}{\partial i_q^*(k)} = \sum_{i=1}^{M} w_{ij}(k-1)\varphi_i(x(k))\frac{c_i(k-1) - i_q^*(k)}{b_i^2(k-1)}. \tag{36}$$

The detailed implementation of the neural network calculation optimization parameter $\beta_i(i=1,2,3)$ is as follows.

B. Fast Fixed-Time Controller Design

Consider system (4) and define the sliding mode manifold as

$$s = x_2 + \frac{1}{\mu(x_1)}(\lambda_1 \text{sig}^{k_1}(x_1) + \lambda_2 h(x_1)) \tag{37}$$

where $\mu(x_1) = a_1 + (1-a_1)\exp(-a_2|x_1|^{a_3})$ and $k_1 = 1 + \frac{m}{2n}(1+\text{sign}(|x_1|-1))$. λ_1, λ_2, a_1, and a_2 are positive values, and $0 < a_1 < 1$. $a_3 > 0$ is an even integer. $m > n > 0$ are two odd integers

$$h(x_1) = \begin{cases} \text{sig}^{k_2}(x_1), & \text{if } \bar{s} = 0 \text{ or } \bar{s} \neq 0,\ |x_1| \geq \kappa \\ \sigma_1 x_1 + \sigma_2 x_1^2 \text{sign}(x_1), & \text{if } \bar{s} \neq 0,\ |x_1| < \kappa \end{cases} \tag{38}$$

where $k_2 = \frac{1}{2}(1+p/q) + \frac{1}{2}(1-p/q)\text{sign}(|x_1|-1)$, $0 < \kappa < 1$, and $0 < p < q$ are two odd integers. $\sigma_1 = (2-p/q)\kappa^{p/q-1}$ and $\sigma_2 = (p/q-1)\kappa^{p/q-2}$

$$\bar{s} = x_2 + \frac{1}{\mu(x_1)}\left(\lambda_1 \text{sig}^{k_1}(x_1) + \lambda_2 \text{sig}^{k_2}(x_1)\right). \tag{39}$$

Taking the time derivative of (37) yields

$$\dot{s} = \dot{x}_2 + \frac{x_2}{\mu(x_1)}\left[\lambda_1 k_1 |x_1|^{k_1-1} + \lambda_2 \dot{h}(x_1)\right] - \frac{1}{\mu^2(x_1)}\left[\dot{\mu}(x_1)\left(\lambda_1 \text{sig}^{k_1}(x_1) + \lambda_2 h(x_1)\right)\right] \tag{40}$$

$$\dot{h}(x_1) = \begin{cases} k_2|x_1|^{k_2-1}, & \text{if } \bar{s}=0 \text{ or } (\bar{s}\neq 0 \text{ and } |x_1| \geq \kappa) \\ \sigma_1 + 2\sigma_2|x_1|, & \text{if } \bar{s}\neq 0 \text{ and } |x_1| < \kappa. \end{cases} \tag{41}$$

To make the system states converge to the proposed sliding mode manifold (37) from arbitrary initial conditions, a reaching law designed as

$$\dot{s} = -\frac{1}{\mu(s)}\left(\lambda_3 \text{sig}^{k_3}(s) + \lambda_4 \text{sig}^{k_4}(s)\right) - k_d \text{sign}(s) \tag{42}$$

where $\mu(s) = b_1 + (1-b_1)\exp(-b_2|s|^{b_3})$, $k_3 = 1 + \frac{m_1}{2n_1}(1+\text{sign}(|s|-1))$, and $k_4 = \frac{1}{2}(1+p_1/q_1) + \frac{1}{2}(1-p_1/q_1)\text{sign}(|s|-1)$. λ_3, λ_4, b_1, b_2, and b_3 are positive values, and $0 < b_1 < 1$. $q_1 > p_1 > 0$ and $m_1 > n_1 > 0$ are four odd integers. $k_d > M$ is the switching gain.

By substituting (42) into (37), the fixed-time sliding mode control law can be acquired as

$$u = \frac{1}{\chi}\left[-\hat{d} - \frac{x_2}{\mu(x_1)}\left(\lambda_1 k_1 |x_1|^{k_1-1} + \lambda_2 \dot{h}(x_1)\right) + \frac{\dot{\mu}(x_1)}{\mu^2(x_1)}\left(\lambda_1 \text{sig}^{k_1}(x_1) + \lambda_2 h(x_1)\right) - \frac{1}{\mu(s)}\left(\lambda_3 \text{sig}^{k_3}(s) + \lambda_4 \text{sig}^{k_4}(s)\right) - k_d \text{sign}(s)\right]. \tag{43}$$

C. Stability Analysis

Theorem 1: Considering the motor system (4), the sliding mode manifold (37) is chosen as the proposed nonsingular fast fixed-time control, and the control law is taken as (43), then after T_r, the closed-loop system is practically fixed-time stable.

Proof: The proof is split into two parts.

Part 1: Select one candidate Lyapunov function as $V_1 = \frac{1}{2}s^2$, and taking the time derivative of V_1 yields

$$\dot{V}_1 = -s\left(\frac{1}{\mu(s)}(\lambda_3 \text{sig}^{k_3}(s) + \lambda_4 \text{sig}^{k_4}(s)) + k_d \text{sign}(s) + d - \hat{d}\right)$$

$$\leqslant -\frac{s}{\mu(s)}(\lambda_3 \mathrm{sig}^{k_3}(s)+\lambda_4 \mathrm{sig}^{k_4}(s))+(M-k_d)|s|$$

$$\leqslant -\frac{1}{\mu(s)}\lambda_3(2V_1)^{(k_3+1)/2}-\frac{1}{\mu(s)}\lambda_4(2V_1)^{(k_4+1)/2}. \quad (44)$$

When $|s| \geqslant 1$, one has

$$\dot{V}_1 \leqslant -\frac{1}{\mu(s)}\lambda_3 2^{(L_2+2)/2}V_1{}^{(L_2+2)/2}-\frac{1}{\mu(s)}\lambda_4 2V_1 \quad (45)$$

and when $|s|<1$, (44) becomes

$$\dot{V}_1 \leqslant -\frac{1}{\mu(s)}\lambda_3 2V_1-\frac{1}{\mu(s)}\lambda_4 2^{(r_2+1)/2}V_1{}^{(r_2+1)/2} \quad (46)$$

where $L_2=\frac{m_1}{n_1}$ and $r_2=\frac{p_1}{q_1}$.

Since $\frac{(L_2+2)}{2}>1$, the first expressions in (14) and (45) are equivalent in form. Similarly, since $\frac{(r_2+1)}{2}<1$, the second expressions in (14) and (46) are also equivalent in form. Consequently, it follows from Lemma 3 that the system states can reach the sliding surface $s=0$ within a fixed time:

$$T_1=\frac{1}{\lambda_4 L_2}\ln\left(1+\frac{\lambda_4}{2^{\frac{L_2}{2}}\lambda_3}\right)+\frac{1}{\lambda_3(1-r_2)}\ln\left(1+\frac{\lambda_3}{2^{\frac{r_2-1}{2}}\lambda_4}\right). \quad (47)$$

Part 2: When $s=0$, the sliding-mode manifold can be denoted as

$$s=x_2+\frac{1}{\mu(x_1)}\left(\lambda_1 \mathrm{sig}^{k_1}(x_1)+\lambda_2 h(x_1)\right)=0. \quad (48)$$

Once the sliding-mode manifold (37) is reached, the following three cases should be analyzed.

Case 1: If $\bar{s}=0$ is reached, it implies that $s=x_2+\frac{1}{\mu(x_1)}(\lambda_1 \mathrm{sig}^{k_1}(x_1)+\lambda_2 \mathrm{sig}^{k_2}(x_1))=0$.

Select one candidate Lyapunov function as $V_2=\frac{1}{2}x_1^2$, and taking the derivative of V_2 versus time yields

$$\dot{V}_2=x_1x_2=-x_1\frac{1}{\mu(x_1)}(\lambda_1 sig^{k_1}(x_1)+\lambda_2 sig^{k_2}(x_1))$$

$$=-\frac{1}{\mu(x_1)}(\lambda_1|x_1|^{k_1+1}+\lambda_2|x_1|^{k_2+1})$$

$$\leqslant -\frac{1}{\mu(x_1)}\lambda_1(2V_2)^{(k_1+1)/2}-\frac{1}{\mu(x_1)}\lambda_2 2V_1{}^{(k_2+1)/2}. \quad (49)$$

When $|x_1| \geqslant 1$, one has

$$\dot{V}_2 \leqslant -\frac{1}{\mu(x_1)}\lambda_1 2^{(L_1+2)/2}V_2{}^{(L_1+2)/2}-\frac{1}{\mu(x_1)}\lambda_2 2V_2 \quad (50)$$

and when $|x_1|<1$, (49) becomes

$$\dot{V}_2 \leqslant -\frac{1}{\mu(x_1)}\lambda_1 2V_2-\frac{1}{\mu(x_1)}\lambda_2 2^{(r_1+1)/2}V_2{}^{(r_1+1)/2} \quad (51)$$

where $L_1=\frac{m}{n}$ and $r_1=\frac{p}{q}$.

Since $\frac{(L_2+1)}{2}>1$, the first expressions in (14) and (50) are equivalent in form. Similarly, since $\frac{(r_1+1)}{2}<1$, the second expressions in (14) and (51) are also equivalent in form. Consequently, according to Lemma 3, it is shown that the system state can converge to origin with a fixed time T_2, and the convergence time T_2 is

$$T_2=\frac{1}{\lambda_2 L_1}\ln\left(1+\frac{\lambda_2}{2^{\frac{L_1}{2}}\lambda_1}\right)+\frac{1}{\lambda_3(1-r_1)}\ln\left(1+\frac{\lambda_1}{2^{\frac{r_1-1}{2}}\lambda_2}\right). \quad (52)$$

When state variable x_1 settles down to the origin, the state variable x_2 also converges to zero. In this case, the settling time T is given by

$$T<T_{\max}=T_1+T_2. \quad (53)$$

Case 2: If $\bar{s}\neq 0$ and $|x_1|\geq\kappa$, according to (37), one has $s=x_2+\frac{1}{\mu(x_1)}(\lambda_1 \mathrm{sig}^{k_1}(x_1)+\lambda_2 \mathrm{sig}^{k_2}(x_1))=0$. According to Lemma 3, it can be concluded that the state x_1 will converge to the region $|x_1|<\kappa$ within a bounded time given by (53). With the convergence of x_1, x_2 also converges to the region $|x_2|\leq\frac{\lambda_1}{\mu(x_1)}\kappa^{k_1}+\frac{\lambda_2}{\mu(x_1)}\kappa^{k_2}=\Phi_1$, $\Phi_1>0$.

Case 3: If $\bar{s}\neq 0$ and $|x_1|<\kappa$, one has $s=x_2+\frac{1}{\mu(x_1)}(\lambda_1 \mathrm{sig}^{k_1}(x_1)+\lambda_2\sigma_1 x_1+\sigma_2 x_1^2 \mathrm{sign}(x_1))=0$. Hence, the following inequality is obtained:

$$|x_2| \leqslant \frac{1}{\mu(x_1)}(\lambda_1|x_1|^{k_1}+\lambda_2(\sigma_1|x_1|+\sigma_2 x_1^2))=\Phi_2 \quad (54)$$

where $\Phi_2>0$.

Based on the previous analysis, it is shown that the system state can converge to $R=\{(x_1,x_2):|x_1|\leq\kappa,|x_2|\leq\max\{\Phi_1,\Phi_2\}\}$ within fixed time $T_{\max}$.

The proof of Theorem 1 is completed.

To clearly show the implementation of the proposed control algorithm, a schematic diagram of the automatic parameter tuning ESO-based fast fixed-time nonsingular terminal sliding mode is provided in Fig. 3.

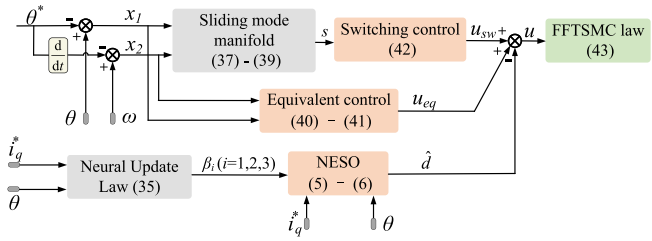

Fig. 3. Schematic diagram of the automatic parameter tuning ESO-based fast fixed-time nonsingular terminal sliding mode control.

D. Control Parameter Selection

The implementation of the proposed approach, the work of tuning or choosing the control gains, to achieve higher pointing accuracy and acceptable control effort, should be carefully done. The following details should be followed when choosing gains.

1) For the parameters a_1, a_2, and a_3, where $0<a_1<1$, $a_2>0$, $a_3>0$, and a_3 is an even number, reducing a_1 or increasing a_2 and a_3 can lead to a decrease in $\mu(x_1)$, thereby accelerating the convergence rate. For b_1, b_2, and b_3, the same pattern applies.

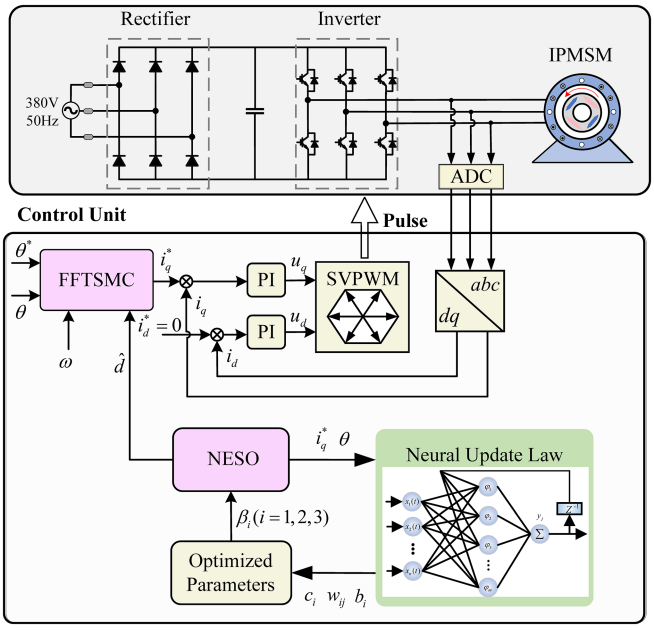

Fig. 4. Block diagram of the proposed control scheme for the PMSM system.

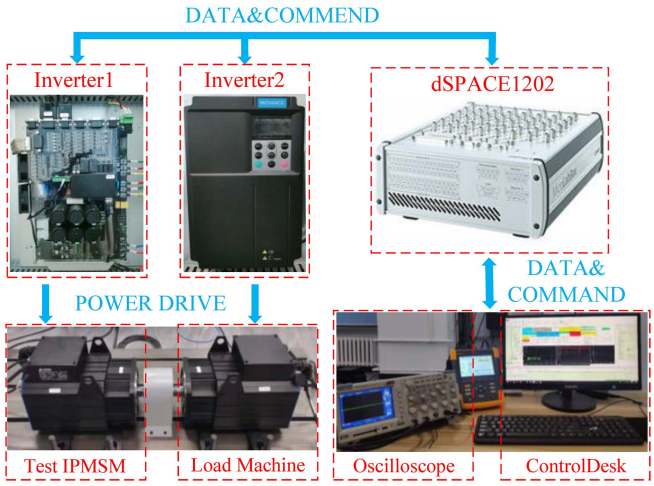

Fig. 5. Test bench of the PMSM.

2) The convergence rate increases with the increase of the values of λ_1, λ_2, λ_3, and λ_4. However, the excessive value will cause the extra chattering and overshoot.
3) The parameters m, n, p, and q will also affect the convergence rate of the tracking error. Usually, $m > n > 0$ and $q > p > 0$. Moreover, a larger m/n or a smaller p/q expedites the convergence rate. Initially, a suitable set of control parameters is selected to ensure the normal operation of the PMSM. To further improve the convergence performance, λ_1, λ_2, λ_3, λ_4, and m/n are appropriately increased individually while keeping the other parameters unchanged. Conversely, these values should be reduced when the overshoot occurs. For m_1, n_1, q_1, and p_1, the same pattern applies.
4) When $x_1 > \kappa$, the proposed sliding mode manifold (37) can provide a faster convergence rate, so κ should be a small positive number. However, when $\kappa = 0$, it leads to a singularity issue.
5) Increasing the parameter k_d enhances the system's disturbance rejection capability. However, a larger value of k_d can introduce chattering issues. Therefore, taking into account chattering effects and control input amplitude, the parameter k_d must be carefully determined through multiple trials.

IV. Experimental Results

The system block diagram is established, as shown in Fig. 4. The PMSM test bench is shown in Fig. 5, which comprises two motors, two drivers, a dSPACE 1202 real-time controller, and corresponding ControlDesk software, where one motor is the motor applied to the proposed method, and the other is used to provide the load torque. Both sampling and control frequency are set to 10 kHz in the experiment. The parameters of the PMSM are given in Table I. To further validate the superiority and effectiveness of the proposed methods, a comparative analysis is conducted on the control performance of the FTSMC method [28], the proposed FFTSMC method, and the proposed FFTSMC + NESO method in the motor servo system. The compared method FTSMC is constructed as [28]

TABLE I
Parameters of the Experimental Platform

Symbol	Descriptions	Values	Unit
p_n	Number of pole pairs	4	-
ψ_f	Flux linkage	0.432	Wb
L_q	q-axis stator inductance	14.14	mH
L_d	d-axis stator inductance	9.32	mH
R_s	Stator resistance	0.602	Ω
J	The moment of inertia	70	kg·cm^2

$$s = e_1 + \left(\frac{1}{\alpha_1 e_1^{\frac{m}{n}-\frac{p}{q}} + \beta_1} e_2\right)^{\frac{q}{p}} = e_1 + (ke_2)^{\frac{q}{p}} \tag{55}$$

$$u = -\frac{1}{\chi}\left[\alpha_1\left(\frac{m}{n}-\frac{p}{q}\right)e_1^{\frac{m}{n}-\frac{p}{q}-1} k e_2^2 - \frac{p}{q}k^{-\frac{q}{p}} e_2^{2-\frac{q}{p}} - k_d \text{sign}(s) - \ddot{\theta}^* - \frac{p}{q}k^{-\frac{q}{p}}\left(\alpha_2 s^{\frac{m_1}{n_1}} + \beta_2 s^{\frac{p_1}{q_1}}\right)\right] \tag{56}$$

where $e_1 = \theta^* - \theta$, $e_2 = \dot{\theta}^* - \omega$, and $k = (\alpha_1 e_1^{m/n-p/q} + \beta_1)^{-1}$.

The complete selection procedure is provided in [28]. For a fair comparison study, the parameters α_2, β_2, and k_d are same as those of the proposed FFTSMC method. The parameters of the controllers are given in Table II.

To assess the performance of the three controllers, sinusoidal and point-to-point motion trajectories are evaluated in the subsequent experiment.

TABLE II
EXPERIMENTAL PARAMETERS

Controllers	Parameters and Values
FTSMC	$m = 13, n = 7, p = 5, q = 7, k_d = 200,$ $m_1 = 11, n_1 = 7, p_1 = 9, q_1 = 7,$ $\alpha_1 = 1, \beta_1 = 20, \alpha_2 = 8, \beta_2 = 8$
FFTSMC	$a_1 = b_1 = 0.8, a_2 = b_2 = 10,$ $a_3 = b_3 = 2, m = m_1 = 5, n = n_1 = 3,$ $p = p_1 = 5, q = q_1 = 9, k_d = 200,$ $\kappa = 0.05, \lambda_1 = \lambda_2 = 2, \lambda_3 = \lambda_4 = 8$
Neural Networks	$\eta = 0.01, \alpha = 0.05$

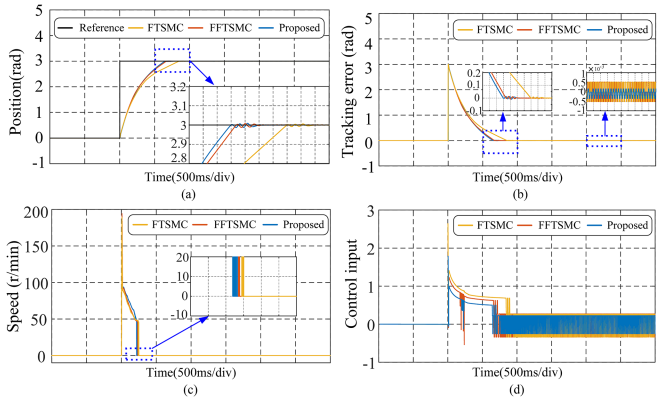

Fig. 6. Experimental results of different control methods under step response. (a) Position tracking results. (b) Tracking errors. (c) Speed response. (d) Control input.

A. Comparative Experiment of Step Response Position Tracking Performance

To demonstrate the superiority of the proposed method, this section compares the position tracking performance and load disturbance rejection capability of various control methods during a position step response. Fig. 6 presents the experimental results of different control methods under a position step response. As shown in Fig. 6, the proposed FFTSMC demonstrates superior convergence performance compared to FTSMC. In addition, Fig. 6 shows that the proposed FFTSMC + NESO effectively reduces system chattering. Fig. 7 shows the dynamic responses of the motor position under different control methods when a load torque of 2 N · m is suddenly applied. The experimental results, as shown in Fig. 7, clearly indicate that both FTSMC and FFTSMC are unable to accurately track the load following a sudden increase, which results in a steady-state error. However, the proposed FFTSMC + NESO method is able to quickly return to 3 rad and exhibits a shorter recovery time. Meanwhile, Table III provides the settling time and steady-state root-mean-square error (RMSE) for evaluating the control performance of the three methods.

Fig. 8 illustrates the process of parameter optimization for the neural network algorithm, with the initial values of β_1, β_2, and β_3 set to 100, 1000, and 1000, respectively. Fig. 8 shows that the proposed parameter optimization method can automatically adjust the control parameters according to different operating

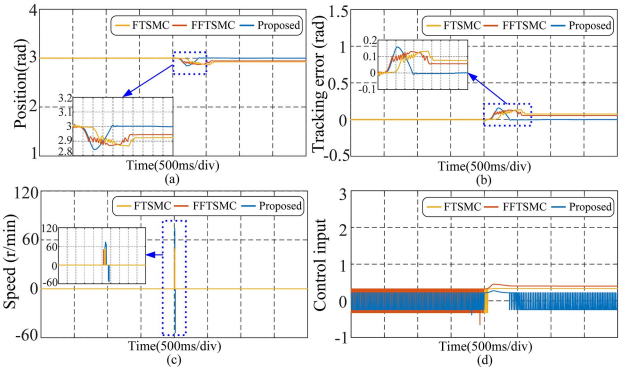

Fig. 7. Experimental results of different control methods under step response with sudden load increase conditions. (a) Position tracking results. (b) Tracking errors. (c) Speed response. (d) Control input.

TABLE III
DETAILED RESULTS OF POSITION RESPONSES FOR DIFFERENT CONTROL METHODS UNDER STEP RESPONSE

Groups	Controllers	Settling time (s)	RMSE
Fig.6	FTSMC	0.85	0.0006
	FFTSMC	0.67	0.0006
	Proposed	0.65	0.0003
Fig.7	FTSMC	0.50	0.078
	FFTSMC	0.48	0.066
	Proposed	0.32	0.0006

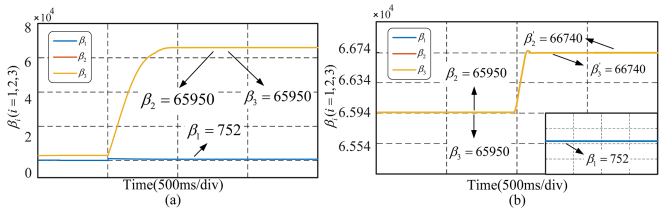

Fig. 8. Experiment results of the parameter optimization under different conditions. (a) Without load. (b) Sudden increase in load.

conditions. Meanwhile, the parameters β_1, β_2, and β_3 satisfy the stability condition, i.e., $\beta_1\beta_2 > \beta_3$ [32].

B. Comparative Experiment of Sinusoidal Response Position Tracking Performance

In this section, the reference outputs of the system are set as a sine wave, and experimental comparisons are conducted between the proposed FFTSMC + NESO, FFTSMC, and FTSMC methods. As shown in Fig. 9, the reference position is $\theta^* = 3 + 2\sin(\pi)$ rad. It can be seen from Fig. 9 that the proposed FFTSMC + NESO method has less steady-state error during the position tracking. In addition, as demonstrated in Fig. 10, the FTSMC method with $k_d = 200$ results in an unstable system state following a sudden load increase during the loading experiment. Consequently, k_d value for the FTSMC method is adjusted to 400, while $k_d = 200$ value for the proposed FFTSMC method remains unchanged. This adjustment demonstrates that

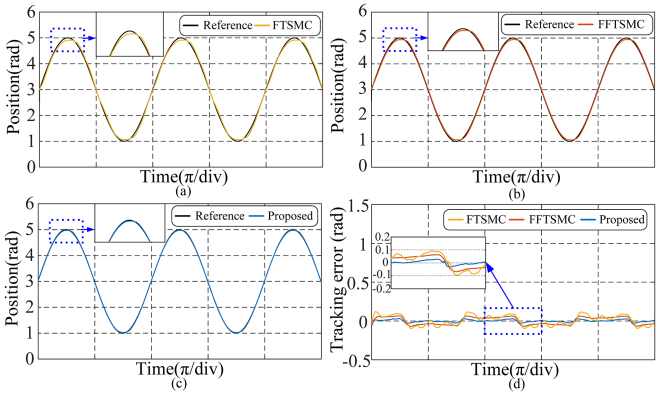

Fig. 9. Experimental results of different control methods under sinusoidal response. (a) Position tracking of FTSMC. (b) Position tracking of FFTSMC. (c) Position tracking of proposed FFTSMC+NESO. (d) Tracking errors of the three methods.

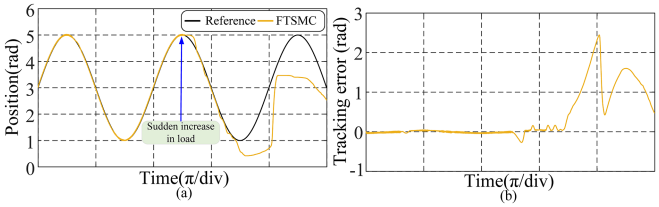

Fig. 10. Experimental results of the FTSMC methods with $k_d = 200$ under sinusoidal response with sudden load increase conditions. (a) Position tracking results. (b) Tracking errors.

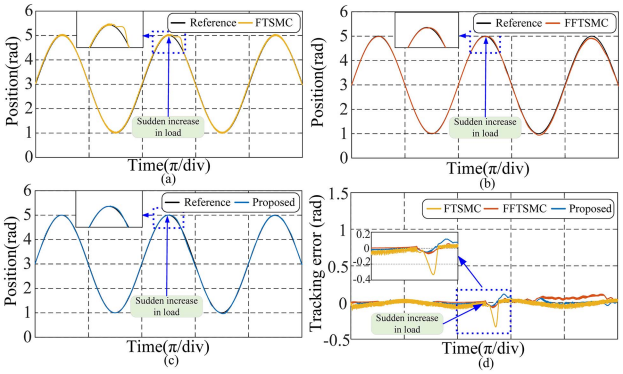

Fig. 11. Experimental results of different control methods under sinusoidal response with sudden load increase conditions. (a) Position tracking of FTSMC ($k_d = 400$). (b) Position tracking of FFTSMC. (c) Position tracking of proposed FFTSMC+NESO. (d) Tracking errors of the three methods.

the proposed FFTSMC method exhibits greater robustness than the FTSMC method with the same k_d value.

As shown in Fig. 11, the reference position is $\theta^* = 3 + 2\sin(\pi)$ rad and the motor is loaded with 2 N · m at $t = 3\pi$ s. The proposed FFTSMC + NESO method demonstrates high tracking accuracy and can quickly converge to a specified position, even in the presence of abrupt changes in the external load, as shown in Fig. 11. Fig. 11(d) reveals that the proposed FFTSMC + NESO method exhibits the smallest fluctuation in position tracking error. The control input responses of the three

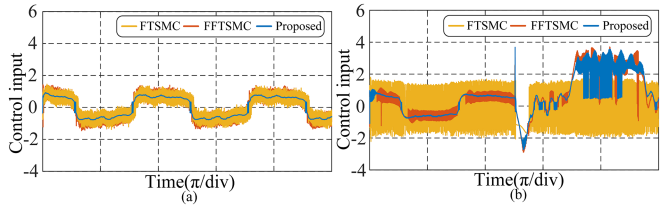

Fig. 12. Experiment results of the control input under different conditions. (a) Without load ($k_d = 200$ of FTSMC). (b) Sudden increase in load ($k_d = 400$ of FTSMC).

TABLE IV
DETAILED RESULTS OF POSITION RESPONSES FOR DIFFERENT CONTROL METHODS UNDER SINUSOIDAL RESPONSE

Groups	Controllers	Maximum tracking errors	RMSE
Fig.9	FTSMC	0.2176	0.0650
	FFTSMC	0.1349	0.0483
	Proposed	0.0618	0.0150
Fig.11	FTSMC	0.3827	0.0525
	FFTSMC	0.2558	0.0412
	Proposed	0.1238	0.0255

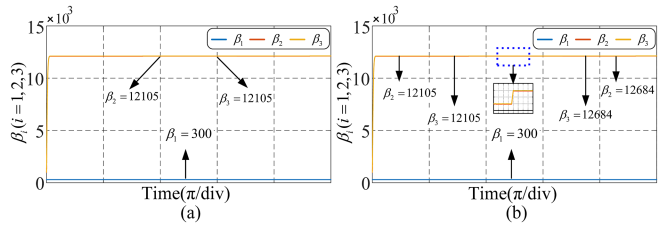

Fig. 13. Experiment results of the parameter optimization under different conditions. (a) Without load. (b) Sudden increase in load.

control methods are shown in Fig. 12, where it can be seen that the proposed FFTSMC+NESO effectively reduces system chattering. In addition, Table IV provides the maximum absolute value of the position tracking errors and RMSE for evaluating the control performance of the three methods. In Fig. 13, the parameter optimization results under sinusoidal response are shown, indicating that the NESO with a parameter optimization mechanism can enhance the system's adaptability to the current operating conditions.

V. CONCLUSION

In this article, a fast fixed-time control method based on parameter self-tuning ESO is proposed, which improves the control performance of the position tracking system under load disturbances. Theoretical analysis and simulation results have verified that the proposed novel fixed-time stabilization system has a faster convergence rate. The proposed parameter optimization mechanism validates on a PMSM experimental platform, demonstrating its capability to automatically optimize and adjust NESO parameters across various operating conditions. Experimental results indicate that, under both step and sinusoidal response conditions, the proposed control method tracks reference commands more quickly and accurately than

other advanced fixed-time control methods. In addition, load experiments demonstrate the method's robustness to disturbances. Therefore, in industrial automation systems requiring high-precision position control, such as computerized numerical control machines and robotic arms, the proposed control strategy can significantly improve system stability and accuracy under unknown disturbances. Future research should focus on improving high-precision position tracking of motors under extreme conditions to ensure optimal performance in challenging operational environments.

REFERENCES

[1] B. Chen, K. Wang, and Y. Le, "High-precision position error correction method for the PMSM based on low-order harmonic suppression," *IEEE Trans. Power Electron.*, vol. 36, no. 4, pp. 4500–4512, Apr. 2021.

[2] W. Lu et al., "Load adaptive PMSM drive system based on an improved ADRC for manipulator joint," *IEEE Access*, vol. 9, pp. 33369–33384, Feb. 2021.

[3] H. Li, S. Yang, and Y. Le, "Torque ripple minimization of low-speed gimbal servo system using parameter-optimized ESO," *IEEE Trans. Emerg. Sel. Topics Power Electron.*, vol. 11, no. 2, pp. 2094–2103, Apr. 2023.

[4] J. Song, W. X. Zheng, and Y. Niu, "Self-triggered sliding mode control for networked PMSM speed regulation system: A PSO-optimized super-twisting algorithm," *IEEE Trans. Ind. Electron.*, vol. 69, no. 1, pp. 763–773, Jan. 2022.

[5] H. Wang, S. Xu, and H. Hu, "PID controller for PMSM speed control based on improved quantum genetic algorithm optimization," *IEEE Access*, vol. 11, pp. 61091–61102, Jun. 2023.

[6] X. Fu, X. Yang, P. Zanchetta, M. Tang, Y. Liu, and Z. Chen, "An adaptive data-driven iterative feedforward tuning approach based on fast recursive algorithm: With application to a linear motor," *IEEE Trans. Ind. Informat.*, vol. 19, no. 4, pp. 6160–6169, Apr. 2023.

[7] C. Yao, G. Ma, Z. Sun, J. Luo, G. Ren, and S. Xu, "Weighting factors optimization for FCS-MPC in PMSM drives using aggregated residual network," *IEEE Trans. Power Electron.*, vol. 39, no. 1, pp. 1292–1307, Jan. 2024.

[8] Y. Wang, S. Fang, J. Hu, and D. Huang, "Multiscenarios parameter optimization method for active disturbance rejection control of PMSM based on deep reinforcement learning," *IEEE Trans. Ind. Electron.*, vol. 70, no. 11, pp. 10957–10968, Nov. 2023.

[9] X. Shen et al., "Sliding-mode control of neutral-point-clamped power converters with gain adaptation," *IEEE Trans. Power Electron.*, vol. 39, no. 8, pp. 9189–9201, Aug. 2024.

[10] A. Polyakov, "Nonlinear feedback design for fixed-time stabilization of linear control systems," *IEEE Trans. Autom. Control*, vol. 57, no. 8, pp. 2106–2110, Aug. 2012.

[11] X. Lin et al., "Observer-based fixed-time control for permanent-magnet synchronous motors with parameter uncertainties," *IEEE Trans. Power Electron.*, vol. 38, no. 4, pp. 4335–4344, Apr. 2023.

[12] T. Li, X. Chen, J. Liu, and J. Yu, "Fixed-time adaptive fuzzy control via filter and observer for uncertain nonlinear systems with disturbances and its application in PMSMs," *IEEE Trans. Ind. Electron.*, vol. 71, no. 11, pp. 14712–14721, Nov. 2024.

[13] F. Hu, T. Ma, and X. Su, "Adaptive fuzzy sliding-mode fixed-time control for quadrotor unmanned aerial vehicles with prescribed performance," *IEEE Trans. Fuzzy Syst.*, vol. 32, no. 7, pp. 4109–4120, Jul. 2024.

[14] Z. Zhu, Y. Lin, and Y. Zhang, "Adaptive quasi-fixed-time integral terminal sliding mode control for nonlinear systems," *IEEE Trans. Circuits Syst. II: Exp. Briefs*, vol. 71, no. 3, pp. 1366–1370, Mar. 2024.

[15] X. Liu, C. Jia, and H. Wang, "Practical variable exponent fixed-time nonsingular sliding mode control for nonlinear systems and its applications," *IEEE Trans. Autom. Sci. Eng.*, vol. 22, pp. 10871–10880, Jan. 2025. DOI: 10.1109/TASE.2025.3529832.

[16] L. Chen et al.., "Sensorless fixed-time sliding mode control of PMSM based on barrier function adaptive super-twisting observer," *IEEE Trans. Power Electron.*, vol. 39, no. 3, pp. 3037–3051, Mar. 2024.

[17] X. Wang and S. Wang, "Fixed-time integral terminal sliding mode control with super-twisting nonlinear extended state observer for servo system with disturbances," *IEEE J. Emerg. Sel. Topics Ind. Electron.*, vol. 6, no. 1, pp. 435–446, Jun. 2025.

[18] X. Yang et al., "Fixed-time generalized super-twisting controller for the trajectory tracking of unmanned surface vehicles in autonomous berthing," *IEEE Trans. Ind. Electron.*, vol. 72, no. 5, pp. 5300–5311, May 2025.

[19] X. Wang, L. Pan, Y. Tian, Y. Liu, and L. Li, "Adaptive fault-tolerant fixed-time sliding mode tracking control for steer-by-wire system with dual-three-phase PMSM," *IEEE Trans. Veh. Technol.*, vol. 74, no. 5, pp. 7554–7564, May, 2025.

[20] C. Jia, X. Liu, and L. Du, "Adaptive second-order fixed-time nonsingular terminal sliding mode control based on barrier function for nonlinear systems," *IEEE Trans. Ind. Informat.*, vol. 20, no. 3, pp. 4806–4815, Mar. 2024.

[21] X. Shen et al., "Fixed-time sliding mode control for NPC converters with improved disturbance rejection performance," *IEEE Trans. Ind. Informat.*, vol. 21, no. 6, pp. 4476–4487, Jun., 2025, doi: 10.1109/TII.2025.3540481.

[22] H. Qin, J. Si, N. Wang, and L. Gao, "Fast fixed-time nonsingular terminal sliding-mode formation control for autonomous underwater vehicles based on a disturbance observer," *Ocean Eng.*, vol. 270, Feb. 2023, Art. no. 113423.

[23] B. Li, H. Liu, C. K. Ahn, C. Wang, and X. Zhu, "Fixed-time tracking control of wheel mobile robot in slipping and skidding conditions," *IEEE/ASME Trans. Mechatron.*, early access, May, 30, 2024, doi: 10.1109/TMECH.2024.3401069.

[24] Z. Liu, J. Liu, O. Zhang, Y. Zhao, W. Chen, and Y. Gao, "Adaptive disturbance observer-based fixed-time tracking control for uncertain robotic systems," *IEEE Trans. Ind. Electron.*, vol. 71, no. 11, pp. 14823–14831, Nov. 2024.

[25] Z. Liu et al., "Fixed-time sliding mode control for dc/dc buck converters with mismatched uncertainties," *IEEE Trans. Circuits Syst. I: Reg. Papers*, vol. 70, no. 1, pp. 472–480, Jan. 2023.

[26] L. Yu, G. He, X. Wang, and S. Zhao, "Robust fixed-time sliding mode attitude control of tilt trirotor UAV in helicopter mode," *IEEE Trans. Ind. Electron.*, vol. 69, no. 10, pp. 10322–10332, Oct. 2022.

[27] M. Gao, L. Ding, and X. Jin, "Elm-based adaptive faster fixed-time control of robotic manipulator systems," *IEEE Trans. Neural Netw. Learn. Syst.*, vol. 34, no. 8, pp. 4646–4658, Aug. 2023.

[28] J. Wang, J. Rong, and J. Yang, "Adaptive fixed-time position precision control for magnetic levitation systems," *IEEE Trans. Autom. Sci. Eng.*, vol. 20, no. 1, pp. 458–469, Jan. 2023.

[29] X. Lin et al., "Observer-based prescribed performance speed control for PMSMs: A data-driven RBF neural network approach," *IEEE Trans. Ind. Informat.*, vol. 20, no. 5, pp. 7502–7512, May 2024.

[30] C. Dai, T. Guo, J. Yang, and S. Li, "A disturbance observer-based current-constrained controller for speed regulation of PMSM systems subject to unmatched disturbances," *IEEE Trans. Ind. Electron.*, vol. 68, no. 1, pp. 767–775, Jan. 2021.

[31] Z.-L. Zhao and B.-Z. Guo, "A nonlinear extended state observer based on fractional power functions," *Automatica*, vol. 81, pp. 286–296, Jul. 2017.

[32] Y. Ma, T. Qin, and Y. Li, "Nonlinear extended state observer based super-twisting terminal sliding mode synchronous control for parallel drive systems," *IEEE/ASME Trans. Mechatron.*, vol. 28, no. 6, pp. 3087–3098, Dec. 2023.

Ruiqi Xu (Graduate Student Member, IEEE) received the B.S. degree in automatic control from Dalian Jiaotong University, Dalian, China, in 2018, and the M.S. degree in automatic control from Lanzhou Jiaotong University, Lanzhou, China, in 2021. He is currently working toward the Ph.D. degree in Control Science and Engineering with Harbin Institute of Technology, Harbin, China.

His current research interests include control of electrical drive systems and advanced control strategy of an electric machine.

Jianxing Liu (Senior Member, IEEE) received the B.S. degree in mechanical engineering and the M.E. degree in control science and engineering from the Harbin Institute of Technology, Harbin, China, in 2004 and 2010, respectively, and the Ph.D. degree in automation from the Technical University of Belfort-Montbeliard, Belfort, France, in 2014.

He is currently a Professor with the Department of Control Science and Engineering, Harbin Institute of Technology. His current research interests include sliding mode control, nonlinear control and observation, industrial electronics, and renewable energy solutions.

Dr. Liu is currently an Associate Editor for several journals, including IEEE/CAA JOURNAL OF AUTOMATICA SINICA, IEEE TRANSACTIONS OF CIRCUITS AND SYSTEMS II: EXPRESS BRIEFS, IEEE SYSTEMS JOURNAL, *Nonlinear Dynamics*, *ISA Transactions*, and IEEE JOURNAL OF EMERGING AND SELECTED TOPICS IN INDUSTRIAL ELECTRONICS. He is also an Associate Editor of the Conference Editorial Board, IEEE Control Systems Society.

Xinpo Lin (Member, IEEE) received the B.S. degree in electrical engineering and automation from the Harbin Institute of Technology, Weihai, China, in 2017, and the M.S. degree in electrical engineering and the Ph.D. degree in control engineering from the Harbin Institute of Technology, Harbin, China, in 2019 and 2024, respectively.

From 2022 to 2023, he was a Visiting Ph.D. Student with the Department of Electrical Engineering, KTH Royal Institute of Technology, Stockholm, Sweden. In 2024, he joined the Harbin Institute of Technology, Weihai, as a Lecturer. His research interests include nonlinear control and observer technology for electrical machine drives.

Zhuang Liu (Member, IEEE) received the B.S. degree in electrical engineering and automation from the China University of Mining and Technology, Xuzhou, China, in 2017, and the M.S. degree in electrical engineering and the Ph.D. degree in control science and engineering from the Harbin Institute of Technology, Harbin, China, in 2019 and 2024, respectively.

From 2022 to 2023, he was a Visiting Scholar with the Department of Mechanical and Production Engineering, Aarhus University, Aarhus, Denmark. He is currently an Associate Research Fellow with the Department of Control Science and Engineering, Harbin Institute of Technology. His current research interests include adaptive control, fixed-time control, and their applications to robotic and power electronic systems.

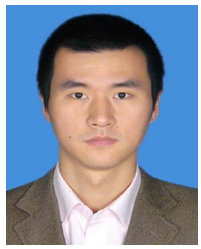

Fei Yan (Member, IEEE) received the B.S. and M.S. degrees in mechanical engineering and automation from Northwestern Polytechnical University, Xi'an, China, in 2004 and 2007, respectively, and the Ph.D. degree in automation from the Technical University of Belfort-Montbeliard, Belfort, France, in 2012.

He is currently a Professor with the School of Information Science and Technology, Southwest Jiaotong University, Chengdu, China. His research interests include control theory and engineering, artificial intelligence, and intelligent transportation systems.

Yabin Gao (Member, IEEE) received the B.M. degree in information management and information systems and the M.E. degree in software engineering from Bohai University, Jinzhou, China, in 2012 and 2015, respectively, and the Ph.D. degree in control science and engineering from the Harbin Institute of Technology, Harbin, China, in 2020.

He is currently an Professor with the Department of Control Science and Engineering, Harbin Institute of Technology. His research interests include cyber-physical systems, multiagent systems, reliable and safe control, intelligent control, and their applications.